

Active Echo: A New Paradigm for Ultrasound Calibration

Xiaoyu Guo, Alexis Cheng, Haichong K. Zhang, Hyun-Jae Kang,
Ralph Etienne-Cummings, and Emad M. Bector

The Johns Hopkins University, Baltimore, MD 21218, USA
{xguo9, acheng22, hzhang61, hjkang, retienne}@jhu.edu,
ebector1@jhmi.edu

Abstract. In ultrasound-guided medical procedures, accurate tracking of interventional tools with respect to the US probe is crucial to patient safety and clinical outcome. US probe tracking requires an unavoidable calibration procedure to recover the rigid body transformation between the US image and the tracking coordinate system. In literature, almost all calibration methods have been performed on passive phantoms. There are several challenges to these calibration methods including dependency on ultrasound image quality and parameters such as frequency, depth, and beam-thickness. In this work, for the first time we introduce an active echo (AE) phantom for US calibration. The phantom actively detects and responds to the US beams from the imaging probe. This active approach allows reliable and accurate identification of the ultrasound image mid-plane independent of the image quality. It also enables automatic point segmentations. Both the target localization and segmentation can be done automatically, so the user dependency is minimized. The AE phantom is compared with a gold standard crosswire (CW) phantom in a robotic US experimental setup. The result indicates that AE calibration phantom provides a localization precision of 223 μm , and an overall reconstruction error of 850 μm . Auto-segmentation is also tested and proved to have the similar performance as the manual segmentation.

1 Introduction

Ultrasound (US) imaging systems are widely integrated with tracking or robotic systems in medical procedures for tool tracking and image guidance. To integrate US with a tracking system and perform more advanced forms of guidance, an US calibration process must be performed. The US transducer must be fixed to a rigid body that can be tracked in some external coordinate system. The tracking is usually done by an optical marker, an electromagnetic (EM) sensor or the robot end-effector. The US calibration process finds the rigid body transformation relating the tracker to the US image, allowing an US image to be positioned in the tracking system base frame. Once calibrated, the US image is registered with any other tools or devices that are also being tracked in this base frame. Thus more advanced uses of the US system are possible, such as overlaying the image onto a video stream or actuating a tracked

robotic actuator to target a region within the US image. The main drawback for US is its poor image quality relative to the other imaging modalities. This drawback often makes it difficult to accurately and automatically segment regions of interest.

To find the transformation between the end-effector frame and the US image frame X , a specialized model or phantom with known configurations is required. A cross-wire (CW) is one of the most commonly used phantom for US calibration [1]. With two wires crossing at a single point, it is a typical form of BXp US calibration, in which a single fiducial is imaged by a tracked US probe in different poses [2-5]. In this equation p is the fiducial point in the sensor coordinate, B is the transformation measured by the tracking system, and X is the unknown desired homogeneous transformation. Since all (B_i, B_j) pairs are measured for the same physical point, the relationship $B_i X p_i = B_j X p_j$ holds for all combinations of i and j . Figure 1a shows the situation where US images of the CW point are accumulated in various poses. One then uses these poses and the segmented points in the US images to reconstruct a single point in the external tracker's space. A limitation that prevents one from getting good calibration accuracy using this method is the US image plane thickness. In US imaging, the US beam transmitted from a probe usually has a width of several millimeters to centimeters dependent on the depth and other imaging parameters. As a result, it is difficult to distinguish whether an object in the B-mode image is intersecting the mid-plane. Since the localization and segmentation completely rely on the US image in conventional calibration phantoms, the elevation axis positioning uncertainty coupled with the relatively low quality of US image result in a reconstruction precision that can easily be worse than a few millimeters. Moreover, this is a user dependent procedure as the operator's experience greatly affects the calibration accuracy.

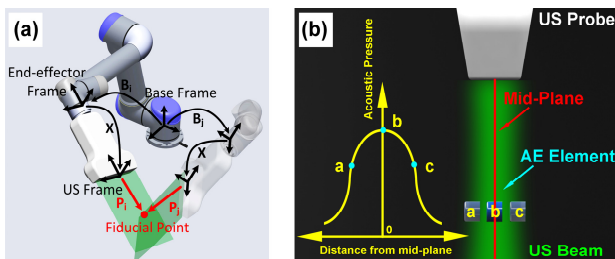


Fig. 1. a) The coordinate transformation in the BXp calibration using a robotic arm as the tracking system. The US probe is attached to the arm, and the B_i is measured from the robot encoders. b) Using AE element for the mid-plane localization. At position b , AE element receives the maximum ultrasound signal amplitude. At a and c , although the element is still shown US image, the received signal amplitude is lower compared to b .

Guo et al [6] demonstrated an interventional tool tracking and guiding technique active ultrasound pattern injection system (AUSPIS), and solves both the object visualization and mid-plane error problem at the same time. In AUSPIS, an active echo (AE) element, which acts as a miniaturized US transducer, is integrated with the target object that needs to be tracked in US images. An electrical system composed of a US receiver, a signal processor, and a pulser is connected to the AE element.

When the US system is acquiring a B-mode image, probe elements fire sequentially to scan the entire field of view (FOV). An AE element in the FOV will sense the beacon pulse when the transmission beam scans over. To improve the tool visualization, the AUSPIS will drive the AE element to send a US pulse immediately after the beacon reception. Since the reception-transmission delay is in nanoseconds and negligible for US imaging, the US pulse is superimposed on the reflected wave, resulting in an enhanced echo pulse with a much higher amplitude, configurable frequency and wider emission angle. This wave travels back to the imaging probe and appears as a bright spot (AE spot) that indicates the AE element location in the B-mode image. Another function of AUSPIS localize the US mid-plane by measuring the local US signal intensity, as shown in figure 1b.

Since the AE element is a point that can be localized in US image accurately, especially along the elevation axis, it is possible to use it in the same way as the CW point for US calibration. Practically, one procedure of finding the mid-plane can be done in three steps. The first step is to move the US probe until the AE element is shown in the B-mode image. The second step is to finely adjust the probe position until the AE element fires active US pulses, which is an indication that the received signal amplitude exceeds the pre-selected AE response threshold. The final step is to increase the threshold and adjust the probe position at the same time, until reaching a position that any small adjustment from this position will stop the active echo response. Another procedure of finding the mid-plane is to use the virtual pattern injection technique. AUSPIS measures the beacon intensity and injects a corresponding number of virtual bars into the B-mode image to indicate the signal strength. Mid-plane can be localized by simply moving the probe and finding the maximum number of bars. With the mid-plane detection feedback from AUSPIS, a more accurate and user independent positioning accuracy can be achieved along the elevation axis, thus we expect a better and more consistent calibration precision using this method.

In this paper, section 2 details the experiment procedures and the data analysis methods. In section 3 the experimental setup is described. The results are shown in section 4 followed by a discussion in section 5.

2 Methods

There were several hypothesis that we wanted to test by performing several CW and AE experiments. The first hypothesis is that the localization of AE points within the ultrasound image mid-plane is more user-independent than the CW points. To test this hypothesis, we conducted an experiment where users repeatedly approached the CW and AE points respectively using the robot-actuated ultrasound probe. The robot motion was restricted to a single dimension such that the two points pass a similar region of the ultrasound beam transmission profile. In this experiment, the user would stop the robot motion and record the robot pose when they felt the AE or CW point was accurately in the ultrasound image's mid-plane. A total of thirty-five poses were recorded for the AE and CW points respectively. From our initial hypothesis, we would

expect the standard deviation of the robot poses to be smaller when imaging the AE point than when imaging the CW point.

The second hypothesis is that the calibration done using AE points is less affected by segmentation errors than when using CW points. To test this hypothesis, we collected sixty CW point and sixty AE point images with their respective robot poses. Two users segmented each of the two data sets by manually choosing the wire cross and AE element points on B-mode images, and repeated for a total of ten times. The ten CW data sets and the ten AE data sets were independently used to solve for X , the transformation relating the robot end effector to the ultrasound image plane. We used a variant of the gradient descent solver described by Ackerman et al. [7] with a cost function that minimizes every pair of $|B_i X p_i - B_j X p_j| = 0$. This resulted in ten X s each using either the CW points or AE points. The repeatability of these ten X s was tested using a version of the method described by Treece et al. [8]. The US image corners are transformed by each X and the standard deviations of the resulting point clouds at each corner is reported with $\forall i, \text{norm}(\text{std}(\{X_i c_i, \dots, X_m c_i\}))$. It is expected that these standard deviations will be lower for the X s computed using the AE points.

The third hypothesis is that the calibration using AE points has a better point reconstruction precision than a calibration using CW points. To test this, we used the segmented points and the X s acquired to test the second hypothesis. Each set of segmented CW points are used to test each of the AE X s and vice versa. The point reconstruction precision is computed by $\text{norm}(\text{std}(\{B_i X p_i, \dots, B_k X p_k\}))$. For example, to compute this metric for the AE X , the robot poses imaging the crosswire and corresponding points would be B and p respectively. We compare the AE X and the CW X with the best reconstruction precisions in their respective sets. The expectation is that the AE X will have a better reconstruction precision. The datasets collected for the fourth and fifth hypothesis were also used to test this hypothesis.

Before we describe the fourth hypothesis, we introduce two additional components used in the experiment. The first is the use of fiber optical hydrophone points as the test data set. By principle, any US sensor can be used as a reception-only AE element for mid-plane localization. Since the mid-plane position is determined by the detected spatial acoustic pressure distribution, a smaller sensor has higher spatial resolution, and results in a higher mid-plane detection accuracy. Fiber optical hydrophones have an effective aperture of as small as 10 μm , and were previously shown by Guo et al. [6] to have better localization than the PZT AE points. Using these points as the point reconstruction test points allow us to further isolate the error in the calibration X from other errors. The second is the automatic segmentation. The active phantom is able to provide both US and electrical feedback when the US probe is aligned with the target point. This enables several methods, like the beacon delay method, frequency modulation method, and time modulation method, to segment the points automatically by the electronics or software. In this paper, we focus on the first one, and leave the other methods for future investigation. In the beacon delay method, the US system outputs two TTL triggers for the RF line and frame synchronization. The AE electronic system receives these two triggers and compare them with the signal received by the AE element. For the axial direction, the system measures the delay between a line trigger and the corresponding beacon signal received by the AE element to get the time of

flight (TOF). So the axial distance can be determined by multiplying the TOF with the speed of sound. Practically, the AE element may receive signals from multiple neighboring RF lines, the system will use the one with the shortest delay as the TOF. For the lateral direction, once a frame trigger is received, the device will start counting the number of line triggers until a TOF is received, and the count will be recorded as n_{tof} . So the axial distance can be determined by $y = L_{probe} * n_{tof} / n_{total}$, where the L_{probe} is the array length, and the n_{total} is the total line triggers in each frame. By using this method, the point segmentation becomes entirely image and user-independent.

The fourth hypothesis is that the automatically segmented AE points result in a calibration comparable to manual CW and AE expert segmentation. To test this, we compare the point reconstruction precisions of the CW X, AE X, and the automatically segmented AE X with our third experimental dataset using sixty optical hydrophone points as the test data set.

The final hypothesis is that Xs constructed from subsets of CW data will vary more than Xs constructed from subsets of AE data. To test this, we take some subset of the data and compute a X. We repeat this one hundred times for the CW, the AE, and the auto-segmented AE. The metric we use is the point reconstruction precision.

One important note in the last hypothesis is that the subset of data for the CW and the AE contain very similar motions. This is only possible with the use of the robot arm as it allows us to have consistent motions between various apparatus. The robot also has a higher accuracy than other tracking system such as electromagnetic or optical trackers. However, the proposed calibration method is generally applicable to other external trackers as well. Moreover, since the system is capable of detecting in-plane conditions, it is possible to trigger the image and tracking data capture automatically once the element is in-plane without holding the probe in position. So it potentially can make the calibration process easier and faster with any tracking system.

3 Experimental Setup

The experiment is performed in a water tank. An AE element and a CW phantom are placed side by side at the same height in the water tank. A Sonix Touch system and a 58.5mm L14-5W probe (Ultrasonix Inc.) is used to acquire a 9 cm depth US image. The probe is attached to a UR5 robotic arm (Universal Robots Inc.), which has 6 degrees of freedom and an end-effector positioning repeatability of $\pm 100\mu\text{m}$. The AE element is made of a customized PZT5H tube with an outer diameter of 2.08mm, an inner diameter of 1.47mm, and a length of 2mm. The electronic system includes a transmit/receive switch, an impedance matching circuit, a variable gain amplifier, filters, a triggering circuit, an analog to digital converter, a microprocessor and a pulser. The CW phantom is made of two 0.2mm fishing lines. A fiber optical hydrophone (OH) developed by Precision Acoustics LTD is also integrated as a reference phantom. This device has a micro Fabry-Pérot acoustic sensor fabricated on a fiber tip [9]. It has a receiving aperture of $10\mu\text{m}$, a bandwidth of 0.25-50 MHz, a dynamic range of 0.01-15MPa, and a sensitivity of 150mV/MPa.

4 Results

The localization precisions as described in the experiment for our first hypothesis are 371 μm and 223 μm for CW and AE, respectively. The localization precision is computed by taking the standard deviations in the robot motion dimension of the recorded robot poses.

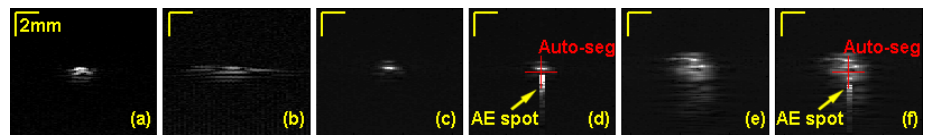


Fig. 2. B-mode images of the CW and AE phantom. a,b) Images of a CW point. c-f) Images of a AE element. a), c) and d) are acquired at 4cm depth, normal angle and in-focus condition. b), d) and f) are acquired at 8cm depth, large incident angle and off-focus condition. d) and f) have the active echo enabled. The auto-segmentation result is also marked on the figure.

Table 1. Repeatability for Xs computed with segmented AE and CW points

Phantom	Corners (Lateral, Axial) (mm)	Repeatability (mm)
AE	(0, 0), (0, 90), (58.5, 0), (58.5, 90)	0.37, 0.60, 0.48, 0.71
CW	(0, 0), (0, 90), (58.5, 0), (58.5, 90)	1.66, 2.82, 1.55, 3.11

Table 2. Best point reconstruction precision for Xs computed with calibration and test data

N = 60	Point Reconstruction Precision (mm)				
Calibrate/ Test Points	AE/CW	AE/Opt	CW/AE	CW/Opt	Auto-AE/Opt
Experiment 2	1.07	0.86	1.72	0.88	
Experiment 3	0.87	0.85	1.08	0.87	0.85

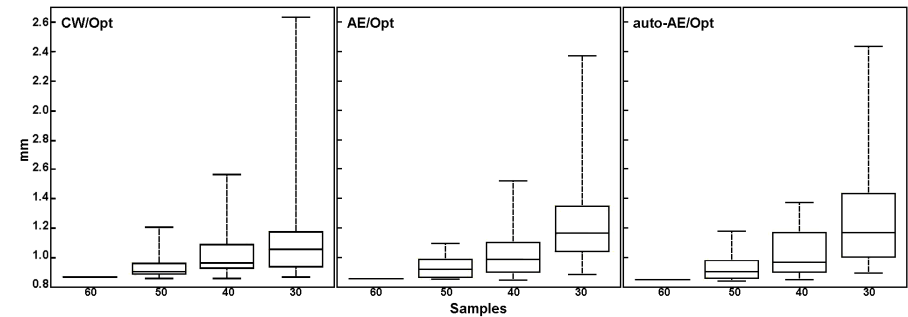


Fig. 3. Comparison of point reconstruction precisions as decreasing sizes of partial data subsets are used for CW, AE, and automatic AE calibration

Table 1 shows the repeatability of the X_s as described in the experiment for our second hypothesis. The corners are chosen to correspond with the ultrasound image dimensions. Three experiments were performed to test our third hypothesis. In the first experiment, the quality of the collected images is low for both CW and AE, mainly due to the multi-reflection and unfocused beam. The data resulted in point reconstruction precisions of 2.36 mm and 1.05 mm for CW and AE, respectively. In experiment 2 and 3, the experimental setup is configured to optimize the image quality. The results are shown in columns AE/CW and CW/OPT in table 2. The results for our fourth hypothesis are also shown in table 2. Data from experiment 1 is not directly compared to 2 and 3 as the difference in image quality.

5 Discussion

The results for our first hypothesis show that the AE points can indeed be localized more precisely in the ultrasound image mid-plane than the CW points. We can see that the localization precision is significantly better for the AE points than the CW points. Also, the results in table 1 show that the X_s computed using different segmentations of the AE images is more repeatable than those of the CW images. This was true for each of the four corners of the ultrasound image.

Table 2 shows that we can achieve comparable point reconstruction precisions using AE calibration and CW calibration. This contradicts our initial hypothesis of better point reconstruction precision. The comparison is especially obvious when we observe table 2 when the same optical hydrophone test set is used for both calibrations. However, we must note here that the current AE setup is not ideal. We were limited by the available piezoelectric components, so the AE element used in this experiment is fairly large in size, resulting in a receiving aperture of around 2mm. This is a major limiting factor that prevents us from getting a higher mid-plane localization accuracy. Also, compared with the CW phantom, AE phantom has the drawback that when the US image plane is far away, it is unable to provide any feedback of the distance. A better implementation in the future could be a hybrid phantom, in which a miniaturized AE element is integrated on the CW. One can then use the wires to guide the probe to the CW point, and use the AE feedback to finely adjust for the mid-plane.

Figure 2 shows the US images of CW and AE phantom under different conditions. For figures 2b, 2e and 2f, the image quality is low and it is difficult to perform accurate manual segmentation. As shown in 2d and 2f, the AE spot can provide a visual cue of the element position, simplifying the manual segmentation. Moreover, image quality dependency can be completely eliminated with auto-segmentation, as shown by the red markers in figures 2d and 2f. In the figure, the marker position is not on the center of the AE element because the image is mainly formed by the top surface of the element. The auto-segmentation marker represents the element's geometric center.

In the auto-segmentation test, we noticed that a few of the auto segmented points are obviously away from the true AE element position by up to 0.4mm. This is mainly because the AE element we use has a cylindrical shape, and does not have a

symmetric signal response along certain angles. As a result, the maximum signal amplitude position deviate from the element geometric center. This may be a possible reason why there is disagreement between the hypothesis and the results in figure 3. In figure 3, the 25th and 75th quartiles are larger for automatic AE than CW for each of the tested number of sample points. Additional experiments will be required as one hundred random subsets of a certain size may not be enough to fully capture its behavior.

The AE system built in our lab includes a customized electronic system and an AE catheter. The overall material cost is less than \$250, which is comparable to a typical 3D printed calibration phantom.

6 Conclusion

In this work, for the first time we demonstrated the use of an active phantom for ultrasound calibration and compared it to conventional CW calibration. We were able to show that AE points could be localized more precisely than CW points. AE calibration was also shown to be less effected by segmentation errors. We showed that AE calibration achieved a point reconstruction precision comparable to CW calibration. Finally, we demonstrated the fully automatic segmentation method with the same point reconstruction precision as manual segmentation. Future work will include the validation of several other proposed automatic segmentation method and the investigation of an optimized AE element design for calibration applications.

References

1. Detmer, P.R., et al.: 3D ultrasonic image feature localization based on magnetic scan head tracking: in vitro calibration and validation. *Ultrasound Med. Biol.* 20(9), 923–936 (1994)
2. Poon, T., et al.: Comparison of calibration methods for spatial tracking of a 3-D ultrasound probe. *Ultrasound Med. Biol.* 31(8), 1095–1108 (2005)
3. Prager, R.W., et al.: *Automatic Calibration for 3-D Free-Hand Ultrasound*, Dep. Eng., Cambridge Univ. (1997)
4. Melvær, E.L., et al.: A motion constrained cross-wire phantom for tracked 2D ultra-sound calibration. *CARS* 7(4), 611–620 (2012)
5. Cleary, K., et al.: Electromagnetic Tracking for Image-Guided Abdominal Procedures: Overall System and Technical Issues. *IEEE EMBS*, 6748–6753 (2005)
6. Guo, X., et al.: Photoacoustic Active Ultrasound Element for Catheter Tracking. In: *SPIE Photonics West* (2014)
7. Ackerman, M.K., et al.: Online Ultrasound Sensor Calibration Using Gradient Descent on the Euclidean Group. In: *International Conference on Robotics and Automation* (2014)
8. Treece, G.M., et al.: High-definition freehand 3-D ultrasound. *Ultrasound Med. Biol.* 29(4), 529–546 (2003)
9. Morris, P., et al.: A Fabry–Pérot fiber-optic ultrasonic hydrophone for the simultaneous measurement of temperature and acoustic pressure. *J. Acoust. Soc. Am* 125(6), 3611 (2009)